PRIMARY PATH ESTIMATOR BASED ON INDIVIDUAL SECONDARY PATH FOR ANC HEADPHONES

Johannes Fabry and Peter Jax

Institute of Communication Systems
RWTH Aachen University
Email: {fabry,jax}@iks.rwth-aachen.de

ABSTRACT

Active noise cancellation (ANC) technology is a valuable asset for hearables. For a well performing and robust ANC system precise knowledge of the relevant acoustic paths is vital. It is feasible to individually measure the user's secondary path by using the inner loudspeaker and microphone that are already built in into most ANC headphones. For measuring the primary path, however, an external loudspeaker as well as a suitable environment for acoustic measurements is required.

We exploit that changes in the primary and secondary path appear jointly, based on the headphone fitting and the physiology of the user's ear. In this contribution, we propose an estimator for the individual primary path based on a measurement of the individual secondary path. We evaluate the estimator by comparing the ANC performance to conventional fixed filter design methods for a large data set of real acoustic paths of an in-ear ANC headphone.

Index Terms— Active noise cancellation, individualization, estimation

1. INTRODUCTION

The large amount of noise pollution in densely populated areas due to, e.g., traffic may lead to stress and even severe psychological and physical illness [1]. For this reason, applications based on active noise cancellation (ANC) technology are a valuable asset for modern hearables [2–5].

Although adaptive algorithms for ANC perform well, they are afflicted by a high computational load [6, 7]. Therefore, the integration of an adaptive ANC system into hearables is not yet feasible due to strict energy and size constraints. State-of-the-art ANC headphones are typically based on fixed feed-forward and feed-back filters and allow for an attenuation of up to 30 dB at low frequencies [8, 9]. The performance of fixed filters is not necessary robust with respect to variations of the headphone fitting and the physiology of the user's ear. An individual design based on measurements of the primary and secondary path can greatly improve the performance and robustness of an ANC system [5, 10]. Most commercially available ANC headphones already come with a built in loudspeaker and two microphones. Thus, it is feasible to measure the secondary path by using the loudspeaker and the inner microphone. The signal-to-noise ratio (SNR) at the inner microphone is quite high due to the passive insulation of the headphone. Different methods for online secondary path estimation exist in literature [7, 11, 12], but are not of interest in this paper as we want to keep the online computational complexity as low as possible. Measuring the primary path, on the other hand, requires an additional external loudspeaker as well as quiet and anechoic surroundings.

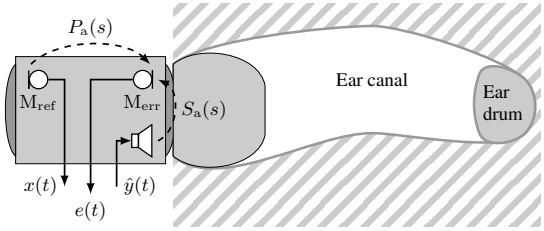

Fig. 1. ANC in-ear headphone topology and acoustic paths.

Measurements of the Bose QC20 in-ear headphone without the ANC electronics [13, 14] show a considerable correlation of primary and secondary paths for different users and fittings. Motivated by this observation, we propose an estimator for the individual primary path based on a measurement of the individual secondary path. The estimator requires offline training on a set of previously measured primary and secondary path pairs. We expect that the approach also works for other headphones, as it is based on changes of the coupled acoustic impedance of the ear canal.

The paper is structured as follows: In Sec. 2 we give a brief overview of the headphone topology as well as the notation we use in this paper. Sec. 3 introduces a method for feed-forward finite impulse response (FIR) filter design for ANC headphones based on a set of previously measured primary and secondary paths as well as the novel primary path estimator. We evaluate and compare the estimator to conventional filter design methods in Sec. 4, using cross-validation on a large data set of real acoustic paths.

2. SYSTEM OVERVIEW

Fig. 1 illustrates the headphone topology that we take as a basis for the scope of this paper. The headphone enclosure contains two microphones and a loudspeaker. The reference microphone $\mathrm{M_{ref}}$ is mounted in the enclosure at the opposing side of the ear canal to record the ambient sound $x(t)$. The error microphone $\mathrm{M_{err}}$ and the loudspeaker face the ear canal. The acoustic primary path $P_\mathrm{a}(s)$ describes the transfer function from $\mathrm{M_{ref}}$ to $\mathrm{M_{err}}$, whereas the acoustic secondary path $S_\mathrm{a}(s)$ describes the transfer function from the loudspeaker to $\mathrm{M_{err}}$. Here, s and z denote the complex frequency parameter of the Laplace- and z-transform, t and n denote the continuous and discrete time, respectively.

Fig. 2 extends the analog model from Fig. 1 by the electronic back-end which is linked to the microphones and the loudspeaker by analog-digital and digital-analog converters (ADC/DAC). Here, $\hat{W}(z)$ is a time-invariant feed-forward FIR filter that receives the ambient

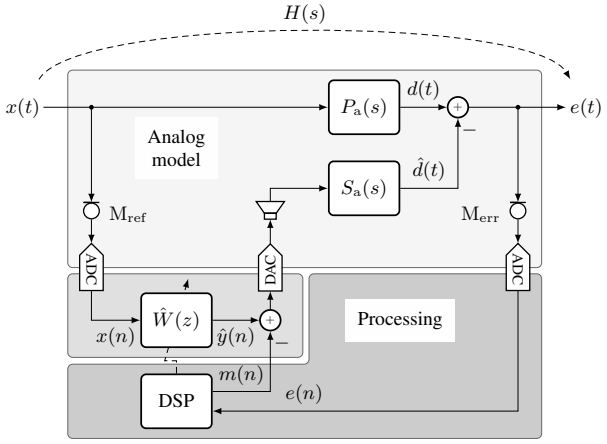

Fig. 2. Block diagram of an feed-forward ANC headphone with hardware components separated into an analog model (▭), a fast digital filter (▭), and a digital signal processor (DSP) (▭).

signal $x(n)$ and creates the cancellation signal $\hat{y}(n)$. The DSP block can play back the measurement signal $m(n)$ and record the error signal $e(n)$ to measure the secondary path. Furthermore, it can update the filter coefficients of $\hat{W}(z)$. The overall transfer function $H(s)$ describes the transfer function from $\mathrm{M_{ref}}$ to $\mathrm{M_{err}}$ and, in contrast to the primary path, includes the influence of the ANC system. In the following, we exclusively use discrete-time data. The primary path $P(z)$ and secondary path $S(z)$ contain the influence of the ADCs, the DAC, the loudspeaker and the microphones, respectively. The overall transfer path is then defined as

$$H(z) = P(z) - W(z)S(z). \tag{1}$$

We note vectors in bold $\boldsymbol{x}$ and matrices in bold and underlined $\underline{\boldsymbol{x}}$. In addition, frequency or z-domain quantities are upper case.

3. FILTER DESIGN

The first subsection introduces a method to feed-forward FIR filter design as described in [5]. Subsequently, in subsection 3.2 we motivate and propose an estimator for the primary path that is trained on a set of previously measured primary and secondary paths. At runtime the estimator receives a measurement of the individual secondary path to estimate the individual primary path.

3.1. Feed-forward filter design

Let $\mathcal{T} = \left\{\boldsymbol{p}_j, \boldsymbol{s}_j \in \mathbb{R}^L \mid j = 1, \ldots, J\right\}$ be a set of measured impulse responses of length L with

$$\boldsymbol{p} = [p(0), p(1), \ldots, p(L-1)]^\mathrm{T} \tag{2a}$$

$$\boldsymbol{s} = [s(0), s(1), \ldots, s(L-1)]^\mathrm{T}. \tag{2b}$$

The optimal feed-forward FIR filter

$$\boldsymbol{w} = [w(0), w(1), \ldots, w(L-1)]^\mathrm{T} \tag{3}$$

minimizes the average of the energy of the overall transfer path, as defined by the cost function

$$\mathcal{C}_\mathrm{w} = \sum_{j\in\mathcal{T}} \left\| \boldsymbol{p}_j^0 - \underline{\boldsymbol{s}}_j \boldsymbol{w} \right\|^2, \tag{4}$$

with the generically defined zero-padded primary path vector

$$\boldsymbol{p}^0 = \left[\boldsymbol{p}^\mathrm{T}, 0, \ldots, 0\right]^\mathrm{T} \in \mathbb{R}^{2L-1} \tag{5}$$

and secondary path convolution matrix $\underline{\boldsymbol{s}} \in \mathbb{R}^{(2L-1)\times L}$

$$\underline{\boldsymbol{s}} = \begin{bmatrix} s(0) & s(1) & \ldots & s(L-1) & 0 & \ldots & 0 \\ 0 & s(0) & \ldots & s(L-2) & s(L-1) & \ddots & \vdots \\ \vdots & \ddots & \ddots & \vdots & \vdots & \ddots & 0 \\ 0 & \ldots & 0 & s(0) & s(1) & \ldots & s(L-1) \end{bmatrix}^\mathrm{T}. \tag{6}$$

The solution to (4) is given by

$$\hat{\boldsymbol{w}} = \arg\min_{\boldsymbol{w}} \mathcal{C}_\mathrm{w} = \left(\sum_{j\in\mathcal{T}} \underline{\boldsymbol{s}}_j^\mathrm{T} \underline{\boldsymbol{s}}_j \right)^{-1} \sum_{i\in\mathcal{T}} \underline{\boldsymbol{s}}_i^\mathrm{T} \boldsymbol{p}_i^0. \tag{7}$$

This solution is optimal but only with respect to the average and not the individual performance. To have optimal individual performance, exact knowledge of $\boldsymbol{p}$ and $\boldsymbol{s}$ is required. It is feasible to measure the individual secondary path $\boldsymbol{s}$ using the loudspeaker and the inner microphone $\mathrm{M_{err}}$ of the headphone. If we substitute the individual secondary path $\underline{\boldsymbol{s}}$ for all $\underline{\boldsymbol{s}}_j$ in (7) and use the ensemble average of the primary paths in $\mathcal{T}$, i.e.,

$$\overline{\boldsymbol{p}} = \frac{1}{J} \sum_{j\in\mathcal{T}} \boldsymbol{p}_j \tag{8}$$

as an estimate for $\boldsymbol{p}$, we obtain the optimal filter based on the individual secondary path:

$$\hat{\boldsymbol{w}}_\mathrm{avg} = \left(\underline{\boldsymbol{s}}^\mathrm{T} \underline{\boldsymbol{s}} \right)^{-1} \underline{\boldsymbol{s}}^\mathrm{T} \overline{\boldsymbol{p}}^0 \tag{9}$$

In the following subsection, we propose an estimator for the individual primary path based on features of the secondary path measurement. Later, in Sec. 4, we compare the performance of the estimator to the filter design using (9).

3.2. Primary path estimator

The primary path $P(z)$ and the secondary path $S(z)$ both depend on the fitting of the headphone and the physiology of the user's ear. This observation results from a large scale measurement series presented in [13]. Fig. 5 shows the magnitude spectra and trends for different fittings of the paths, which we later use for the evaluation in Sec. 4.

We utilize these joint changes to design an estimator for the individual $\boldsymbol{p}$ based on features of a measured individual secondary path $\boldsymbol{s}$. We extract the frequency regions of the transfer functions that are affected by deterministic changes, as highlighted in red in Fig. 5, with respective window functions $Q_\mathrm{p}(z)$ and $Q_\mathrm{s}(z)$ in the z-domain:

$$P_\mathrm{q}(z) = Q_\mathrm{p}(z) P(z), \tag{10a}$$

$$S_\mathrm{q}(z) = Q_\mathrm{s}(z) S(z). \tag{10b}$$

We define the single-sided frequency domain vector

$$\boldsymbol{P}_\mathrm{q} = \left[P_\mathrm{q}\left(e^{j0}\right), P_\mathrm{q}\left(e^{j\frac{2\pi}{L}}\right), \ldots, P_\mathrm{q}\left(e^{j\frac{2\pi}{L}\lfloor\frac{L}{2}\rfloor}\right) \right]^\mathrm{T} \in \mathbb{C}^{\lfloor\frac{L}{2}\rfloor+1}.$$

By principal component analysis (PCA) we extract the first $K_\mathrm{p}, K_\mathrm{s}$ principal components $\boldsymbol{U}_{\mathrm{p},k}, \boldsymbol{U}_{\mathrm{s},k} \in \mathbb{C}^{\lfloor\frac{L}{2}\rfloor+1}$ of the set of windowed,

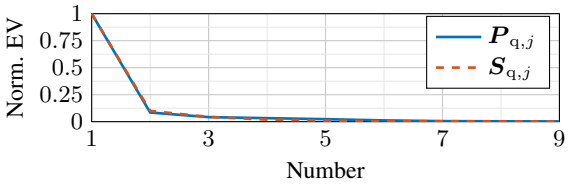

Fig. 3. First 9 normalized eigenvalues (EV) of the singular value decomposition during the PCA of $\boldsymbol{P}_{\mathrm{q},j}, \boldsymbol{S}_{\mathrm{q},j}$.

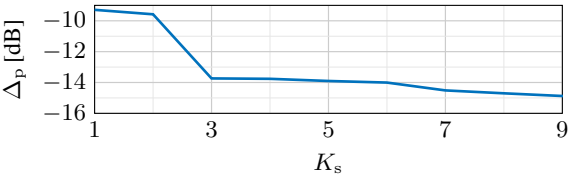

Fig. 4. Relative estimation error Δ_{p} of the primary path gain vector in dB for $K_{\mathrm{p}} = 1$ and different K_{s}.

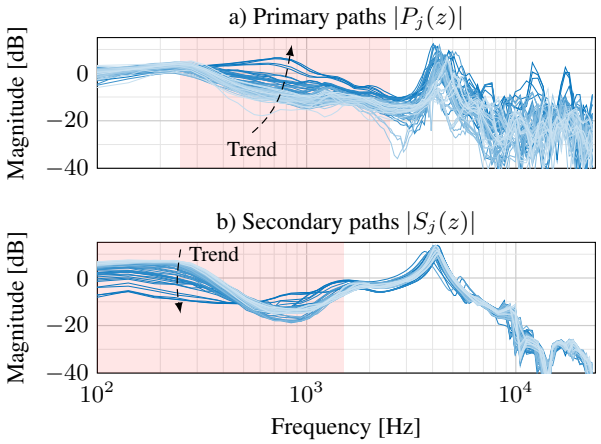

Fig. 5. Magnitude spectra of primary and secondary paths. The highlighted area ( ) shows the frequency range that we use for the window functions $Q_{\mathrm{p}}(z)$ and $Q_{\mathrm{s}}(z)$.

complex frequency domain vectors $\boldsymbol{P}_{\mathrm{q},j}, \boldsymbol{S}_{\mathrm{q},j} \in \mathcal{T}$, respectively. We define the primary path principal components matrix

$$\underline{\boldsymbol{U}}_{\mathrm{p}} = \left[\boldsymbol{U}_{\mathrm{p},1}, \boldsymbol{U}_{\mathrm{p},2}, \ldots, \boldsymbol{U}_{\mathrm{p},K_{\mathrm{p}}}\right]. \tag{11}$$

Again, we define the ensemble average $\overline{\boldsymbol{P}}_{\mathrm{q}}$ of $\boldsymbol{P}_{\mathrm{q},j}$ analogously to (8). To obtain the complex gain vectors $\boldsymbol{g}_{\mathrm{p},j}$ that minimize the Euclidean distance between the reconstructed frequency domain vectors

$$\hat{\boldsymbol{P}}_{\mathrm{q},j} = \overline{\boldsymbol{P}}_{\mathrm{q}} + \underline{\boldsymbol{U}}_{\mathrm{p}} \boldsymbol{g}_{\mathrm{p},j} \tag{12}$$

and the true frequency domain vectors $\boldsymbol{P}_{\mathrm{q},j}$ we make use of the orthonormality of the principal components and get

$$\boldsymbol{g}_{\mathrm{p},j} = \underline{\boldsymbol{U}}_{\mathrm{p}}^{\mathrm{H}} \left(\boldsymbol{P}_{\mathrm{q},j} - \overline{\boldsymbol{P}}_{\mathrm{q}}\right), \tag{13}$$

with the Hermitian transpose $(\cdot)^{\mathrm{H}}$. Similarly we obtain the gains $\boldsymbol{g}_{\mathrm{s},j}$ for the secondary path.

Now, we want to find a linear map $\underline{\boldsymbol{a}} \in \mathbb{C}^{K_{\mathrm{p}} \times K_{\mathrm{s}}}$ that projects the secondary path gain vectors onto the primary path gain vectors. We define the cost function

$$\mathcal{C}_{\mathrm{a}} = \sum_{j \in \mathcal{T}} \left\| \tilde{\boldsymbol{g}}_{\mathrm{p},j} - \underline{\boldsymbol{a}} \tilde{\boldsymbol{g}}_{\mathrm{s},j} \right\|^2, \tag{14}$$

with $\tilde{\boldsymbol{g}} = \boldsymbol{g} - \overline{\boldsymbol{g}}$ and the ensemble average $\overline{\boldsymbol{g}}$. The linear map allows us to estimate the primary path gain vector based on the secondary path gain vector. We minimize $\mathcal{C}_{\mathrm{a}}$ and obtain

$$\hat{\underline{\boldsymbol{a}}} = \arg\min_{\underline{\boldsymbol{a}}} \mathcal{C}_{\mathrm{a}} = \sum_{j \in \mathcal{T}} \tilde{\boldsymbol{g}}_{\mathrm{p},j} \tilde{\boldsymbol{g}}_{\mathrm{s},j}^{\mathrm{H}} \left(\sum_{i \in \mathcal{T}} \tilde{\boldsymbol{g}}_{\mathrm{s},j} \tilde{\boldsymbol{g}}_{\mathrm{s},j}^{\mathrm{H}} \right)^{-1}. \tag{15}$$

Note that the system of equations in (14) is under-determined if $K_{\mathrm{s}} < K_{\mathrm{p}}$. Hence, it is important to choose $K_{\mathrm{s}} \geq K_{\mathrm{p}}$. Fig. 3 shows the first 9 normalized eigenvalues of the singular value decomposition during the PCA of $\boldsymbol{P}_{\mathrm{q},j}, \boldsymbol{S}_{\mathrm{q},j}$. The quick decay of the eigenvalues implies that it is reasonable to reduce the number of components. Therefore, we choose $K_{\mathrm{p}} = 1$. Fig. 4 shows the relative estimation error

$$\Delta_{\mathrm{p}} = \frac{\sum_{j \in \mathcal{T}} \left\| \boldsymbol{g}_{\mathrm{p},j} - \hat{\boldsymbol{g}}_{\mathrm{p},j} \right\|^2}{\sum_{j \in \mathcal{T}} \left\| \boldsymbol{g}_{\mathrm{p},j} \right\|^2} \tag{16}$$

of the primary path gain vector for $K_{\mathrm{p}} = 1$ and different K_{s} and with the estimate according to (17). We see that the estimation error is a monotonically decreasing function of K_{s}. Based on this figure, we choose $K_{\mathrm{s}} = 3$. A linear mapping of the windowed, complex frequency domain vectors $\boldsymbol{P}_{\mathrm{q},j}, \boldsymbol{S}_{\mathrm{q},j}$ is possible but would require a large set of training data. The proposed estimator benefits from numerical robustness and efficiency due to the dimensionality reduction of the PCA.

In summary, the estimator requires the following training steps based on a training set $\boldsymbol{p}_j, \boldsymbol{s}_j \in \mathcal{T}$:

1. Find the frequency domain window functions $Q_{\mathrm{p}}(z), Q_{\mathrm{s}}(z)$ that capture the regions where $P(z), S(z)$ are affected by deterministic changes.
2. Extract the first $K_{\mathrm{p}}, K_{\mathrm{s}}$ principal components from the windowed frequency domain vectors $\boldsymbol{P}_{\mathrm{q},j}, \boldsymbol{S}_{\mathrm{q},j}$ by PCA.
3. Calculate the gain vectors $\boldsymbol{g}_{\mathrm{p},j}$ according to (13) and analogously $\boldsymbol{g}_{\mathrm{s},j}$.
4. Find the linear map $\hat{\underline{\boldsymbol{a}}}$ according to (15).

Then, after measuring the individual secondary path, we apply the window function $Q_{\mathrm{s}}(z)$ in the z-domain and then calculate the gain vector for the secondary path analogously to (13). We then obtain an estimate for $\boldsymbol{g}_{\mathrm{p}}$ by

$$\hat{\boldsymbol{g}}_{\mathrm{p}} = \overline{\boldsymbol{g}}_{\mathrm{p}} + \underline{\boldsymbol{a}} \boldsymbol{g}_{\mathrm{s}} \tag{17}$$

and finally an estimate $\hat{\boldsymbol{P}}$ for $\boldsymbol{P}$ with the ensemble average $\overline{\boldsymbol{P}}$ of $\boldsymbol{P}_j$

$$\hat{\boldsymbol{P}} = \overline{\boldsymbol{P}} + \underline{\boldsymbol{U}}_{\mathrm{p}} \hat{\boldsymbol{g}}_{\mathrm{p}}. \tag{18}$$

We obtain the individual feed-forward filter by replacing $\overline{\boldsymbol{p}}$ with $\hat{\boldsymbol{p}}$ in (9).

4. EVALUATION

To verify the proposed estimator, we conduct simulations on a large scale data set which was obtained by the authors from the measurement series described in [13]. It contains measurements of the Bose QC20 headphone without the ANC electronics for 25 subjects and

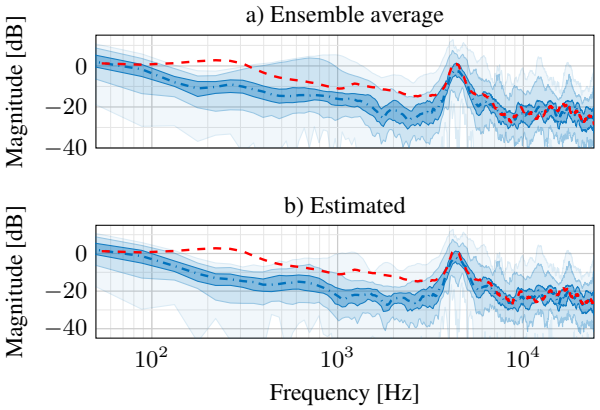

Fig. 6. Median of $|H(z)|$ (-·-·-) and of the primary path $|P(z)|$ (- - -) as well as the 50% ( ), 90% ( ), 100% ( ) percentiles of $|H(z)|$.

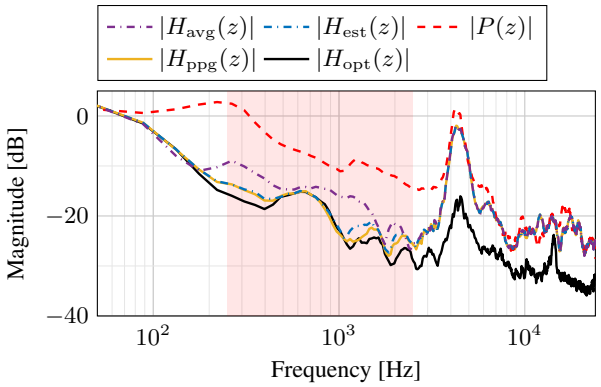

Fig. 7. Median of $|P(z)|$ (- - -) and $|H(z)|$ based on the average primary path (-·-·-), the estimated primary path (-·-·-), the estimated primary path with perfect PCA gains (——) as well as actual primary path (——).

different fittings at a sampling rate of 48 kHz. We define the set $\mathcal{M} = \{\boldsymbol{p}_j, \boldsymbol{s}_j \in \mathbb{R}^L \,|\, j = 1, \ldots, J\}$ of measured primary and secondary paths that contains a total of $J = 173$ impulse response pairs. Fig. 5 shows the magnitude spectra of these primary and secondary path pairs. Each pair is color-coded with the same shade of blue to highlight the joint change and sorted by the energy of the secondary path at low frequencies. The area highlighted in red marks the frequency region for which we designed rectangular frequency domain windows $Q_{\text{p}}(z), Q_{\text{s}}(z)$. We choose the length of the primary and secondary paths to $L = 1024$. The length of the feed-forward filter is $L_{\text{w}} = 64$.

The set is randomly split into two proper subsets $\mathcal{T} \subset \mathcal{M}$ and $\mathcal{V} = \mathcal{M} \setminus \mathcal{T}$, so that $\mathcal{T}$ contains 80% of $\mathcal{M}$, whereas $\mathcal{V}$ contains 20% of $\mathcal{M}$. The subset $\mathcal{T}$ is used to train the estimator as described in Sec. 3.2. We choose $K_{\text{p}} = 1$ and $K_{\text{s}} = 3$, as motivated by Fig. 3 and 4. We then validate the performance of the estimator by investigating the overall transfer path $\boldsymbol{h}_j$ for each impulse response pair from the subset $\mathcal{V}$

$$\boldsymbol{h}_j = \boldsymbol{p}_j^0 - \underline{\boldsymbol{s}}_j \hat{\boldsymbol{w}}, \qquad \forall j \in \mathcal{V}. \tag{19}$$

We repeat this experiment 100 times for randomly split subsets $\mathcal{T}, \mathcal{V}$ and observe the distribution of the magnitude spectrum $|H(z)|$ over all experiments.

Fig. 6 shows the frequency bin-wise median and percentiles of the magnitude spectrum $|H(z)|$ in blue. In a) the filter design is based on the individual secondary paths and the average primary path as in (9). In b) the filter design is based on the individual secondary paths and the estimated primary path according to Sec. 3.2. Furthermore, we added the median of the primary path to show the passive attenuation of the headphone.

Fig. 7 shows the median of the magnitude spectrum $|H(z)|$ for different primary path estimates and individual secondary paths. Here, $H_{\text{avg}}(z)$ is based on the ensemble average from (8), $H_{\text{est}}(z)$ is based on the primary path estimate from (18), $H_{\text{ppg}}(z)$ is also based on the primary path estimate from (3.2) but with the perfect PCA gain (PPG) $\boldsymbol{g}_{\text{p}}$ instead of $\hat{\boldsymbol{g}}_{\text{p}}$, and finally $H_{\text{opt}}(z)$ is based on the individual primary path. The area highlighted in red, where $|Q_{\text{p}}(z)| > 0$, marks the frequency range where $H(z)$ is actually affected by the primary path estimator.

From Fig. 7 we see that the median of the magnitude spectrum $|H(z)|$ reduces by up to 7 dB between 250 Hz and 2.5 kHz and approaches the median of $|H(z)|$ based on the individual primary path. More importantly though, the system performance is significantly more robust as indicated by the 90% and 100% percentiles in Fig. 6.

We define the energy ratio ε of the windowed overall transfer path and the primary path using $Q_{\text{p}}(z)$ as

$$\varepsilon_j = \frac{\oint |H_{\text{q},j}(z)|^2 \, \text{d}z}{\oint |P_{\text{q},j}(z)|^2 \, \text{d}z}. \tag{20}$$

The box plot in Fig. 8 shows the energy ratio in dB for the different primary path estimates analogously to Fig. 7. By using the estimator, the median reduces by 3.1 dB, whereas the difference between the upper whiskers is 5.0 dB.

5. CONCLUSION

In this contribution, we proposed an estimator of the primary path for active noise cancellation (ANC) headphones. The estimator is based on a measurement of the individual secondary path and requires offline training on a set of previously measured primary and secondary paths. We compare the performance of a feed-forward ANC filter design based on estimated primary paths to conventional filter design techniques using cross-validation on a large data set of primary and secondary path pairs. The results show a significant improvement of the robustness of the ANC performance with respect to the fitting of the headphone and the physiology of the user's ear. Also, the overall ANC performance increases.

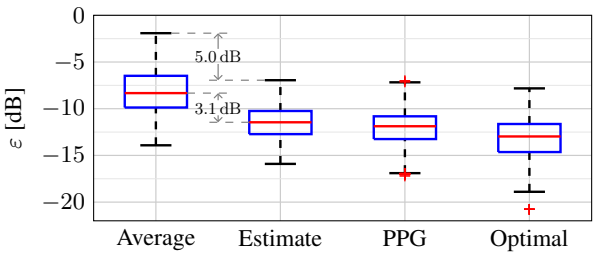

Fig. 8. Boxplot of the energy ratio ε in dB as defined in (20) for different primary path estimates.

6. REFERENCES

[1] World Health Organization (WHO), "Burden of disease from environmental noise: Quantification of healthy life years lost in Europe," 2011.

[2] S. M. Kuo and D. R. Morgan, *Active Noise Control Systems: Algorithms and DSP Implementations*. Hoboken: Wiley, 1996.

[3] A. Bernier and J. Voix, "An active hearing protection device for musicians," in *Proceedings of Meetings on Acoustics ICA2013*, vol. 19, no. 1. ASA, 2013, p. 040015.

[4] K. P. Annunziato, J. Harlow, M. Monahan, A. Parthasarathi, R. C. Silvestri, and E. M. Wallace, "In-ear active noise reduction earphone," Mar. 25 2014, US Patent 8,682,001.

[5] J. Fabry, F. König, S. Liebich, and P. Jax, "Acoustic equalization for headphones using a fixed feed-forward filter," in *ICASSP 2019-2019 IEEE International Conference on Acoustics, Speech and Signal Processing (ICASSP)*. IEEE, 2019, pp. 980–984.

[6] P. A. C. Lopes and M. Piedade, "The Kalman filter in active noise control," in *INTER-NOISE and NOISE-CON Congress and Conference Proceedings*, vol. 1999, no. 5. Institute of Noise Control Engineering, 1999, pp. 1111–1124.

[7] J. Fabry, S. Liebich, P. Vary, and P. Jax, "Active noise control with reduced-complexity Kalman filter," in *16th International Workshop on Acoustic Signal Enhancement (IWAENC)*. IEEE, Sep. 2018.

[8] M. O'Connell, R. Termeulen, and D. M. Gauger Jr, "Systems and methods of active noise reduction in headphones," Aug. 29 2017, US Patent 9,747,887.

[9] S. Liebich, J.-G. Richter, J. Fabry, C. Durand, J. Fels, and P. Jax, "Direction-of-arrival dependency of active noise cancellation headphones," in *ASME 2018 Noise Control and Acoustics Division Session presented at INTERNOISE 2018*. American Society of Mechanical Engineers, 2018, pp. V001T08A003–V001T08A003.

[10] F. Denk, M. Hiipakka, B. Kollmeier, and S. M. A. Ernst, "An individualised acoustically transparent earpiece for hearing devices," *Int. J. Audiol.*, vol. 57, no. sup3, pp. 62–70, 2018.

[11] M. Zhang, H. Lan, and W. Ser, "Cross-updated active noise control system with online secondary path modeling," *IEEE Trans. Speech Audio Process.*, vol. 9, no. 5, pp. 598–602, Jul. 2001.

[12] A. Carini and S. Malatini, "Optimal variable step-size NLMS algorithms with auxiliary noise power scheduling for feedforward active noise control," *IEEE Trans. on Audio, Speech, and Language Process.*, vol. 16, no. 8, pp. 1383–1395, 2008.

[13] J. Fabry, D. Hilkert, S. Liebich, and P. Jax, "Time-variant acoustic front-end measurements of active noise cancellation headphones," in *Proceedings of the 23rd International Congress on Acoustics (ICA)*, DEGA. EAA, Sep. 2019.

[14] S. Liebich, J. Fabry, P. Jax, and P. Vary, "Acoustic path database for ANC in-ear headphone development," in *Proceedings of the 23rd International Congress on Acoustics (ICA)*, DEGA. EAA, Sep. 2019.